PHYSICAL REVIEW B **80**, 165406 (2009)

Determination of the gate-tunable band gap and tight-binding parameters in bilayer graphene using infrared spectroscopy

A. B. Kuzmenko, I. Crassee, and D. van der Marel
Département de Physique de la Matière Condensée, Université de Genève, CH-1211 Genève 4, Switzerland

P. Blake and K. S. Novoselov
Manchester Centre for Mesoscience and Nanotechnology, University of Manchester, Manchester M13 9PL, United Kingdom
(Received 5 August 2009; revised manuscript received 15 September 2009; published 8 October 2009)

We present a compelling evidence for the opening of a bandgap in exfoliated bottom-gated bilayer graphene by fitting the gate-voltage-modulated infrared reflectivity spectra in a large range of doping levels with a tight-binding model and the Kubo formula. A close quantitative agreement between the experimental and calculated spectra is achieved, allowing us to determine self-consistently the full set of Slonczewski-Weiss-McClure tight-binding parameters together with the gate-voltage-dependent bandgap. The doping dependence of the bandgap shows a good agreement with the existing calculations that take the effects of self-screening into account. We also identify certain mismatches between the tight-binding model and the data, which can be related to electron-electron and electron-phonon interactions.

DOI: 10.1103/PhysRevB.80.165406 PACS number(s): 78.30.Na, 78.20.−e, 78.67.Pt, 81.05.Bx

I. INTRODUCTION

Bilayer graphene has recently attracted much attention motivated by a broad spectrum of unusual electronic properties and a number of possibilities for applications. It represents the simplest system, where the effects caused by a coupling between graphene layers can be studied and exploited. Although the interlayer coupling is much weaker than the in-plane chemical bonding, it results in profound differences between electronic and transport properties of monolayer and bilayer graphene, as exemplified by the anomalous quantum Hall effect.[1–3] Another notable dissimilarity is related to the behavior of these systems in a perpendicular electric field. While in zero field both of them are zero-gap semiconductors (or zero-overlap semimetals), in bilayer graphene a bandgap is generated in the presence of the field, due to an introduced asymmetry of the electrostatic potential on the two planes.[4–7] Importantly, the bandgap can be tuned continuously either by applying gate voltage[8] or chemically,[9] which, in combination with a high mobility of charge carriers, opens new unexplored avenues for using bilayer graphene in field-effect transistors[10–12] and other electronic devices.

Using angle-resolved photoemission spectroscopy (ARPES), Ohta *et al.*[9] indeed observed a bandgap in bilayer graphene epitaxially grown on top of silicon carbide and doped chemically with potassium. A more "clean" way of introducing charge carriers is by applying electric field using gate electrodes. This technique can be most easily applied to exfoliated samples, produced by micromechanical cleavage of graphite.[13] Apart from the bandgap generation, applying a gate voltage has also the usual doping effect. In order to control the doping and the bandgap independently, Oostinga *et al.*[8] fabricated two electrodes on both sides of the sample and found an insulating state, when gate voltages of opposite signs were applied to the electrodes. This showed the existence of the bandgap, although the determination of its exact value from the dc measurements was not possible.

Infrared spectroscopy, which is one of the most direct methods to measure the bandgap and other band characteristics in conventional semiconductors, is clearly a technique of choice also in the case of bilayer graphene. The two dimensionality of this material perfectly matches geometrical requirements of an optical experiment. Moreover, the possibility of changing the chemical potential and the bandgap with the gate voltage supplies an unprecedented amount of additional information[14–22] compared to standard optical measurements.

The tight-binding theory is widely used to describe the low-energy π bands in graphitic materials. In the case of graphite, a set of tight-binding parameters, known as the Slonczewski-Weiss-McClure (SWMcC) model,[23,24] was very successful in describing quantitatively the de Haas–van Alphen effect and optical spectra.[25] Therefore, one can expect that it will also apply to bilayer graphene if the bandgap is properly included. It appears that all SWMcC parameters influence the optical conductivity for photon energies below 1 eV. However, the effects of different parameters are rather dissimilar and not all of them can be easily extracted from the spectra.

Several calculations of the optical conductivity of bilayer graphene within the tight-binding approach were done. Nilsson *et al.*[26] and Abergel and Fal'ko[27] considered the simplest model, which contains only the nearest-neighbor (NN) in-plane and interplane hopping terms ($\gamma_0 \sim 3$ eV and $\gamma_1 \sim 0.4$ eV, respectively) and found that the optical conductivity is marked by a profound structure at the photon energy $\hbar\omega \sim \gamma_1$ (we shall refer to this structure as the γ_1 peak). Nicol and Carbotte[28] extended this model to include a bandgap and finite doping. Zhang *et al.*[18] studied the role of additional parameters responsible for the electron-hole asymmetry.

Using infrared techniques, Wang *et al.*[17] observed, in agreement with the aforementioned predictions, a profound anomaly in the spectra of gated bilayer graphene at $\hbar\omega \sim \gamma_1$. Later on, a clear electron-hole asymmetry was found in the infrared spectra by Li *et al.*[19] and by Kuzmenko *et al.*,[20] which allowed determining more SWMcC parameters. However, the presence of the bandgap in these studies, although

expected, was not evident. In Ref. 19 no experimental signatures of the bandgap were reported and in Ref. 20 only a partial agreement between the experimental data and a tight-binding calculation, including a bandgap obtained theoretically,[7] was found. As it will be discussed below, this is explained by the fact that the manifestation of the bandgap in doped graphene is more subtle and, therefore, requires more accurate optical measurements and delicate analysis than in the case of an undoped sample. In the latter case a sharp absorption threshold corresponding to the electron-hole excitations across the gap is expected.

Such a structure was indeed observed by Zhang *et al.*,[22] who measured infrared absorption of double-gated bilayer graphene, where the electric field and doping could be controlled independently.[8] A bandgap of up to 250 meV was observed in an undoped sample in the presence of the largest applied fields, which is a rather promising sign for the use of bilayer graphene in electronics. Although for the large values of the bandgap the match between the experiment and a tight-binding calculation was very close, at low gate voltages, where the absorption threshold was beyond the experimentally accessible range, the quantitative agreement between the experimental and theoretical curves turned out to be rather poor.

In general, the quantitative agreement between infrared spectra of bilayer graphene and tight-binding model was up to now not very good. Apart from the mentioned discrepancies, the measured height of the γ_1 peak in Ref. 18 was about two times larger than the calculated value. Mak *et al.*[21] reported the opening of a bandgap in top-gated bilayer graphene, where a small thickness of the gate insulating layer allowed a rather efficient doping. The quantitative agreement with the tight-binding theory, however, was limited, which the authors attributed to many-body correlation effects.

A common problem that one encounters when analyzing infrared spectra of graphene is their sensitivity to several band parameters, including the bandgap, making their separate extractions quite complicated. Another issue is a possible inhomogeneity of the doping level, which has a similar effect on the optical spectra as an elevated temperature, as will be shown below. In the double-gate experiments, the deposition of the top gate on top of graphene may affect the band structure and increase electronic scattering, not to mention a more complicated optical multilayer model that has to be used in order to extract the optical conductivity of graphene. Therefore, in the present study we fit directly the measured reflectivity spectra of bottom-gated bilayer graphene with a tight-binding model that involves the bandgap, the SWMcC parameters, scattering rate, temperature, and the impurity doping as adjustable parameters. We find that a good quantitative agreement can in fact be achieved, which implies that the band structure of bilayer graphene is well captured by the tight-binding model. Nevertheless, certain discrepancies remain that may eventually be related to many-body effects.

The remaining sections are organized as follows. In Sec. II we describe the sample preparation, infrared experiment, and a specially developed technique of direct fitting of the whole set of reflectivity spectra with a tight-binding model and the Kubo formula. In Sec. III, the results of the infrared measurements, their fits, and the doping dependence of the bandgap and the chemical potential are shown. In Sec. IV we discuss the reliability of extracting the bandgap and compare its gate-voltage dependence with the existing theoretical predictions. We demonstrate a practical way of visualizing important features of the band structures using the experimental reflectivity data. We also discuss the advantages and limitations of the tight-binding model in describing infrared spectra.

II. TECHNIQUES

A. Sample

A relatively large ($\sim$100 μm) flake of bilayer graphene produced by micromechanical cleavage[13] of graphite single crystals on top of a SiO_2 (300 nm)/n-Si substrate was chosen for infrared experiments. Lithographically deposited leads to the flake and the gate (doped silicon) allowed a simultaneous measurement of the dc conductivity σ_{DC} and the infrared reflectivity R as functions of the gate voltage V_g. By sweeping V_g from the positive to the negative values, one continuously varies the doping from electron to hole type. The charge concentration can be determined using the relation $n=\alpha(V_g-V_{CN})$, where the coefficient $\alpha=7.2\times10^{10}$ cm^{-2}/V is given by the electric capacitance of the oxide layer. Usually the charge neutrality point V_{CN} is related to the minimum V_{min} of the $\sigma_{DC}(V_g)$ curve. However, from the fits of the optical spectra described below we found that V_{CN} (which is about -22 V for the presented series of measurements) is slightly different from $V_{min}(\approx-29$ V). It is likely that this is related to the large flake dimensions and a doping inhomogeneity near electrical contacts. Note that here we used devices with only one (bottom) gate for the reasons discussed in Sec. I.

The negative value of V_{CN} is due to charge transfer by adsorbed gas molecules (environmental doping).[29] In order to reduce this effect, the sample was annealed in a H_2-N_2 atmosphere at 150 °C before each series of measurements. Although the annealing indeed shifts V_{CN} closer to the zero bias, we found that, in contrast to the case of monolayer graphene, it never results in $V_{CN}=0$. It is possible that the remaining dopants are located either between the flake and the substrate or are even intercalated between the carbon layers. As we will see below, this correlates with the doping dependence of the bandgap.

B. Optical experiment

Optical reflectivity spectra in the range of photon energies 0.06–1 eV were collected at nearly normal incidence using an IR microscope Bruker Hyperion 2000 attached to a Fourier transform spectrometer with a standard globar source. Appreciable signal could be obtained using the beam spot down to 10–15 μm. However, prior to each series of measurements we optimized in a trial-and-error fashion the spot size in order to maximize the signal-to-noise ratio while avoiding unphysical spectral artifacts related to the finite sample dimensions and apparatus issues. The spectral reso-

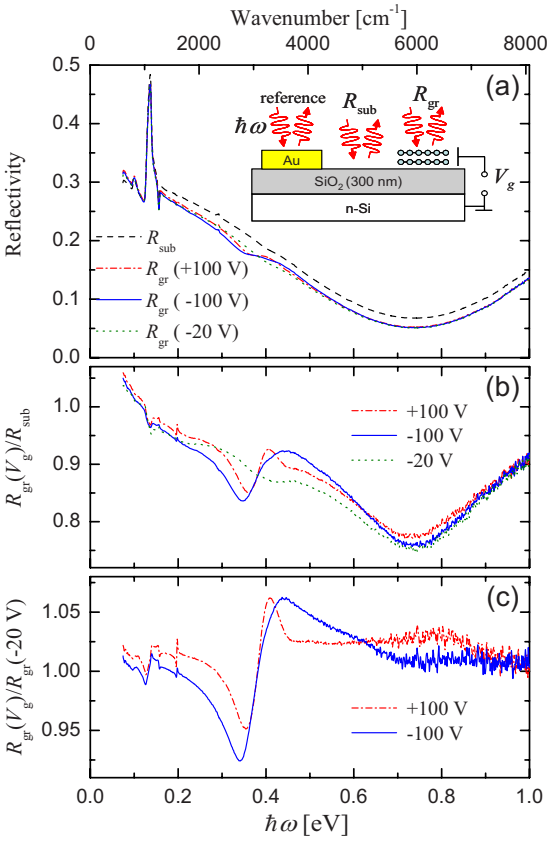

FIG. 1. (Color online) (a) Absolute (gold-normalized) reflectivity of bare oxide and graphene at V_g=+100, −20, and −100 V. The substrate temperature is 10 K. (b) Reflectivity of graphene normalized to bare oxide. (c) Self-normalized reflectivity of graphene $R_{gr}(V_g)/R_{gr}(-20\ \mathrm{V})$.

lution was 1 meV. The sample was mounted in a He flow cryostat; a specially made sample holder allowed us inserting the sample with a minor delay after the annealing.

Absolute reflectivity spectra of the bare substrate $R_{sub}(\omega)$ and the flake $R_{gr}(\omega)$ were obtained using a gold patch deposited near the sample as a reference [Fig. 1(a)]. The substrate and graphene spectra look similar: they all show a prominent minimum at 0.75 eV due to the Fabry-Perot effect in the SiO_2 layer and intense peaks below 0.15 eV originating from dipole-active lattice vibrations in silicon oxide. The change in reflectivity introduced by graphene is better seen in Fig. 1(b), where $R_{gr}(\omega)$ is normalized to $R_{sub}(\omega)$. One can see that graphene introduces a significant infrared contrast, especially close to the Fabry-Perot minimum. Notably, the same effect in the visible range makes graphene detectable by human eyes.[30,31]

From Fig. 1(b) it is also clear that varying the gate voltage has a strong effect on reflectivity. To see it even better, one can normalize R_{gr} by its value at V_g=−20 V, which is close to the charge-neural point [Fig. 1(c)]. Note that the SiO_2 phonon features do not fully cancel after the normalization because of a nonlinear character of the contribution of the substrate to the spectra. At 0.2 eV one can see a sharp structure related to the infrared-active phonon mode in graphene, which has a Fano shape and strongly increases as a function of the gate voltage due to a coupling to electronic interband

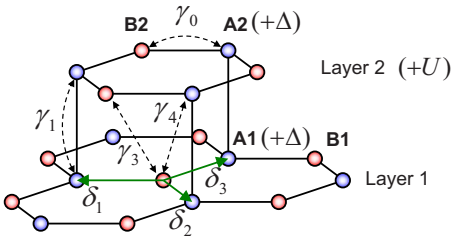

FIG. 2. (Color online) Crystal structure of Bernal-stacked bilayer graphene and the considered tight-binding parameters.

transitions, as discussed in detail in Ref. 32. As we shall see below, the other changes are due to a combination of the doping effect and the opening of the bandgap.

One should note that the diffraction of electromagnetic radiation may affect the measured reflectivity at low energies, where the wavelength becomes comparable to the spot size. Due to the diffraction and other systematic uncertainties, the absolute accuracy of R_{gr} and R_{gr}/R_{sub} is about 0.01–0.02 as we determined by varying the position and the size of the beam spot on the sample. In contrast, the self-normalized reflectivity $R_{gr}(V_g)/R_{gr}(-20\ \mathrm{V})$ can be measured much more accurately (with an uncertainty less than 0.002) since it does not require any reference measurement and, therefore, does not involve any mechanical movements. In order to minimize the influence of weak drifts of the signal, taking spectrum at each gate voltage was immediately followed by a separate measurement at the charge-neutral point.

C. Data modeling

For the data analysis we chose the SWMcC (Refs. 23 and 24) tight-binding description of the π bands in bilayer graphene.[33] We begin with considering it simply as a band-structure parametrization in order to extract information about the electronic bands from the infrared data. Later on we shall discuss the limitations of this description as a physical model based on the quality of the obtained fits.

The structure of the Bernal-stacked bilayer graphene is shown in Fig. 2. Each layer has two sublattices: A1 and B1 (bottom layer) and A2 and B2 (top layer). Atoms A1 and A2 are on top of each other, while the atoms B1 and B2 are shifted horizontally by the vectors $\vec{\delta}_{1,2,3}$ connecting nearest neighbors within one layer. The SWMcC Hamiltonian involves the in-layer nearest-neighbor hopping γ_0 and three interlayer hopping terms: γ_1 (between A1 and A2), γ_3 (between B1 and B2) and γ_4 (between A1 and B2 or between B1 and A2). In addition, the on-site energy difference Δ between the positions A1 and B1 (A2 and B2) is introduced. Following the standard procedure,[4–7,34] we add to the SWMcC model an extra parameter U in order to describe the difference between the (screened) electrostatic potential of the top and the bottom layers in the external field. Note that U gives exactly the separation between the electron and hole bands at the K point and is slightly larger than the true bandgap $\Delta_g \approx |U|\gamma_1/(U^2+\gamma_1^2)^{1/2}$. The exact relation between the gate voltage and the bandgap involves a certain model for the screening, which has been addressed in details, for example, in Refs. 4–7. In the basis $|\mathrm{B1}\rangle$, $|\mathrm{A1}\rangle$, $|\mathrm{A2}\rangle$, and $|\mathrm{B2}\rangle$ the present Hamiltonian reads as follows:

$$H(\vec{q}) = \begin{pmatrix} 0 & \gamma_0\phi & -\gamma_4\phi & \gamma_3\phi^* \\ \gamma_0\phi^* & \Delta & \gamma_1 & -\gamma_4\phi \\ -\gamma_4\phi^* & \gamma_1 & \Delta+U & \gamma_0\phi \\ \gamma_3\phi & -\gamma_4\phi^* & \gamma_0\phi^* & U \end{pmatrix}, \quad (1)$$

where $\phi = e^{i\vec{q}\vec{\delta}_1} + e^{i\vec{q}\vec{\delta}_2} + e^{i\vec{q}\vec{\delta}_3}$ and $\vec{q}$ is the electronic momentum.

Within the linear-response theory, the Kubo formula can be used to calculate the complex optical conductivity $\sigma(\omega)$. In the case of a thin layer, a physically more relevant quantity is the optical sheet *conductance* $G(\omega) = \sigma(\omega)d$, where d is the layer thickness. The total conductance consists of the Drude, the interband, and the high-frequency terms

$$G(\omega) = G_D(\omega) + G_{IB}(\omega) + G_\infty(\omega). \quad (2)$$

The first two terms can be obtained using the expressions

$$G_D(\omega) = \frac{2G_0}{\pi^2}\sum_i \int d^2\vec{q} \left| \langle \vec{q},i| \frac{\partial H}{\partial q_x} |\vec{q},i\rangle \right|^2 \times \left[\frac{-\partial f(\epsilon_{\vec{q},i})}{\partial \epsilon} \right] \frac{i}{\hbar\omega + i\Gamma_D}, \quad (3)$$

$$G_{IB}(\omega) = \frac{2G_0}{\pi^2}\sum_{i,j\neq i} \int d^2\vec{q} \left| \langle \vec{q},i| \frac{\partial H}{\partial q_x} |\vec{q},j\rangle \right|^2 \times \frac{f(\epsilon_{\vec{q},i}) - f(\epsilon_{\vec{q},j})}{\epsilon_{\vec{q},j} - \epsilon_{\vec{q},i}} \frac{i}{\hbar\omega - \epsilon_{\vec{q},j} + \epsilon_{\vec{q},i} + i\Gamma}, \quad (4)$$

where $G_0 = e^2/4\hbar \approx 6.08 \times 10^{-5}\ \Omega^{-1}$ is the universal ac conductance of monolayer graphene[35–38] and graphite,[39] $\epsilon_{\vec{q},i}$ are the electronic band energies, Γ is the electronic broadening parameter and $f(\epsilon) = \{1 + \exp\frac{\epsilon-\mu}{k_BT}\}^{-1}$ is the Fermi-Dirac distribution. The indices i and j count the four bands in bilayer graphene. For the derivation of these formulas we can refer, for example, to Ref. 37, where it was done in the case of monolayer graphene.

The term $G_\infty(\omega)$, which is purely imaginary in the considered spectral range, absorbs contributions from all high-frequency core-level and valence-band electronic transitions, in particular, the ones involving σ bands. We assume that it does not contribute to the doping dependence of the optical spectra.

The chemical potential μ is determined implicitly by the doping level via equation

$$\frac{1}{2\pi^2}\sum_i \int d^2\vec{q} \left[f(\epsilon_{\vec{q},i}) - \frac{1}{2} \right] = n = \alpha(V_g - V_{CN}). \quad (5)$$

We subtract 1/2 in the brackets because the doping level is counted relative to half-filling of the π bands. The spin degeneracy is already included in Eqs. (3)–(5) but the valley degeneracy is not. It appears that for the considered range of energies and temperatures it is sufficient to perform the momentum integration only in a circle of about 1% of the total two-dimensional Brillouin zone around the K point (and multiply by 2 to account for the valley degeneracy). In practical implementation, we replace the integration with a summation over $\sim 10^5$ q points.

In Eqs. (3) and (4) we introduced two different scattering rates for the Drude and the interband components. Above 0.1 eV, the real part of the Drude conductance is much smaller than the imaginary part, and the latter is only very weakly affected by the Drude scattering in this range. Since the data are not sensitive to the Drude scattering rate, we adopted $\Gamma_D = 5$ meV, which corresponds to the value found in graphite.[39] We assume that the interband scattering Γ is constant, *i.e.*, it is independent of energy, momentum, and band index. By doing this, we neglected the energy-dependent electron-phonon and electron-electron-scattering processes, which is perhaps the most serious limitation of the present model. We will see that it is likely in the origin of some deviations of the model curves from the experimental ones.

Once the conductance of graphene is computed, the curves $R_{gr}(\omega)$ can be calculated via the Fresnel equations using the known optical constants of SiO_2 and Si, as specified in the Appendix. The latter values are well known and can be further refined by the fitting of the reflectivity of the bare substrate $R_{sub}(\omega)$.

To summarize, the conductance $G(\omega, V_g)$ and the reflectivity $R_{gr}(\omega, V_g)$ within the presented approach depend on nine parameters: γ_0, γ_1, γ_3, γ_4, Δ, U, Γ, T, and V_{CN}. We applied the nonlinear Levenberg-Marquardt modeling routine[40] to directly fit the experimental spectra. In order to speed up the iterations and improve the convergence, the derivatives of the reflectivity with respect to all adjustable parameters were calculated explicitly using analytical formulas. One obstacle to this approach is that the chemical potential should be determined from Eq. (5), which in general can be done only numerically. Therefore, we treated μ as a fitting parameter and used Eq. (5) as a rigid constraint of the least-square minimization.

III. RESULTS

A. Reflectivity spectra and their tight-binding modeling

As it was discussed in the Sec. II A, the self-normalized reflectivity $R(V_g)/R(-20\ \text{V})$ (from now on we omit the index "gr" for brevity) is the most accurately determined quantity, which is, therefore, the best suitable for quantitative analysis. These spectra, taken at the substrate temperature of 10 K, are presented in Fig. 3(a) for the whole span of gate voltages used (from −100 V to +100 V with a step of 10 V). As compared to Fig. 1(c), the spectral resolution in this figure is diminished to 5 meV. The spectra contain rich structure that evolves in a peculiar fashion as a function of the gate voltage. Such a complicated behavior is due to the fact that all four bands are involved into the electronic transitions that affect optical properties in the considered energy range.

The amplitude of the structures of $R(V_g)/R(-20\ \text{V})$ increases as the difference between V_g and −20 V grows. Therefore, it is useful to also plot the differential reflectivity spectra [Fig. 3(b)] defined as follows:

$$\frac{\Delta R}{R}(\omega, V_g) \equiv 2\frac{R(\omega, V_g + 5\ \text{V}) - R(\omega, V_g - 5\ \text{V})}{R(\omega, V_g + 5\ \text{V}) + R(\omega, V_g - 5\ \text{V})}. \quad (6)$$

Such a way of showing data emphasizes certain structures such as those indicated with dashed lines, and their gate-

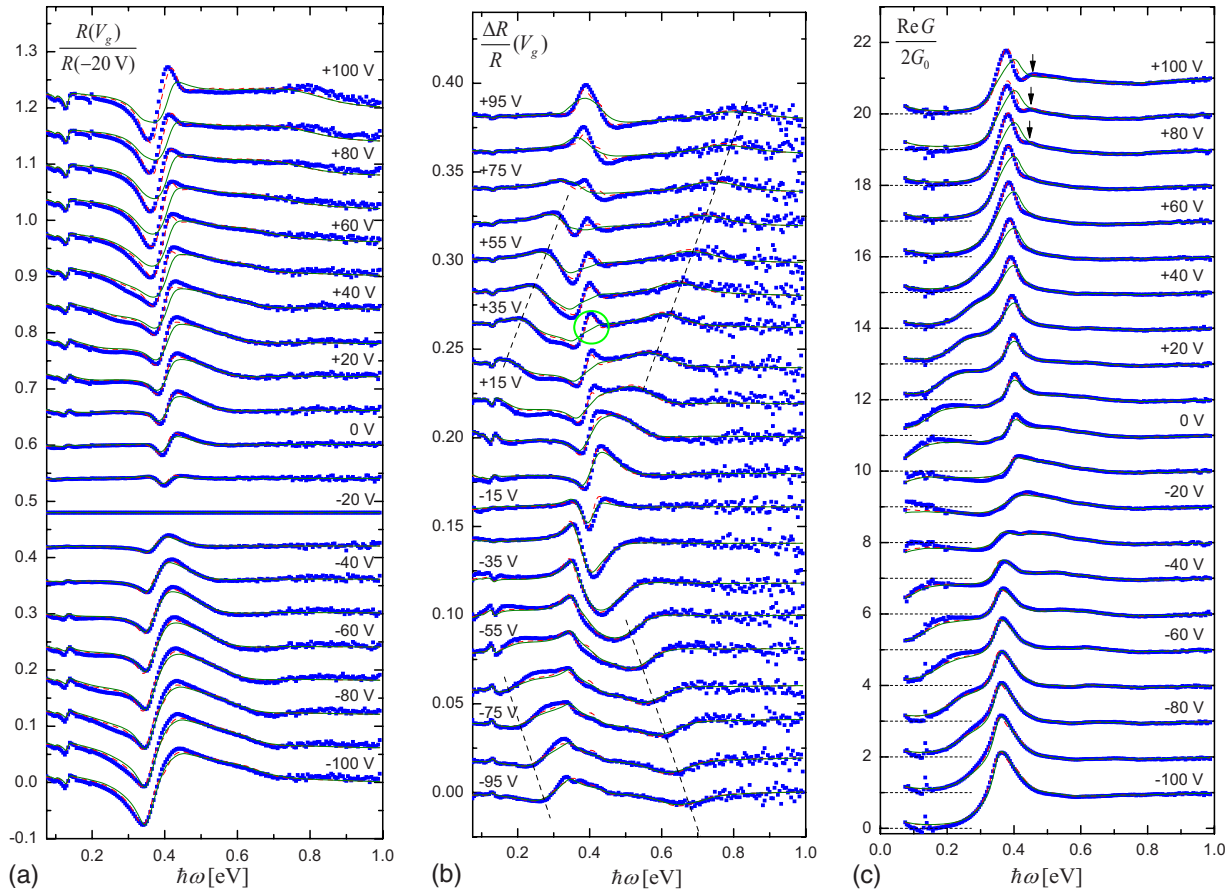

FIG. 3. (Color online) (a) Self-normalized and (b) difference reflectivity spectra as a function of V_g. Dots are the experimental data points, solid and dashed lines represent model fits 1 and 2 (without and with a bandgap), respectively. (c) The real part of the optical conductance. Curves—the result of the reflectivity fits (the colors and the line types correspond to panels a and b), symbols—the refined conductance obtained using a KK-consistent inversion as described in the text. In all panels the curves are vertically displaced for clarity.

voltage dependence. Another advantage of this representation is that it does not require *a priori* the knowledge of the gate voltage corresponding to the charge-neutral state.

We fitted the whole set of the $\Delta R/R$ spectra *simultaneously* using the tight-binding parametrization, described in Sec. II C. We assumed that the γ_0, γ_1, γ_3, γ_4, Δ, Γ, T, and V_{CN} do not depend on V_g. Since one of our main goals is to detect and measure the bandgap, we performed fits in two different ways. First, we set the parameter U to zero at all gate voltages (fit 1) so that the difference between the spectra is only due to a variation in the chemical potential. In the second run (fit 2), the bandgap was allowed to vary as a function of V_g in such a way that U at each value of the gate voltage was treated as an independent parameter. In each case, we tried different sets of initial parameters (within the scope of physically reasonable values) and checked that the fitting routine converges to the same result. The parameter confidence limits were estimated based on the correlation analysis[40] and by repeating the process after varying data points within their error bars.

The model curves corresponding to fits 1 and 2 are shown in Figs. 3(a) and 3(b) (solid green and dashed red lines, respectively). Both fits show almost the same match to the data outside the region around 0.4 eV. However, within this region fit 1, which does not involve the bandgap, is qualitatively worse. It fails to reproduce some strong structures, in particular, the ones marked with the circle. As discussed in Refs. 18, 20, and 28, this is exactly the region, where the bandgap is expected to affect the spectra. At the same time, the quality of fit 2 is remarkably good. Thus our data unequivocally show the presence of the bandgap. There are still some mismatches that we shall address separately.

The parameters of fit 2, apart from U, which depends on the gate voltage, are given in the Table I. One can see that the SWMcC parameters can be determined from the infrared spectra. Except γ_3, these parameters were already determined in previous infrared studies,[17–20] by monitoring the gate-voltage dependence of easily recognizable spectral features such as the maximum of the γ_1 peak. Using the least-square fitting method, the parameter γ_3 can now also be estimated. This term results in a deformation of the γ_1 peak, but its effect on the spectra is more complicated than just a broadening produced by Γ (that we find to be about 18 meV). One should mention, that in fit 1 (where the bandgap was not included) this parameter relaxed to an artificially large value (about 0.5 eV), in order to mimic somehow the bandgap induced smearing of the γ_1 peak.

For comparison, we also reproduce the SWMcC parameters obtained from a density-functional theory (DFT) calculation on graphite by Charlier *et al.*[41] (a more complete over-

TABLE I. Parameter values obtained by the least-square fitting of reflectivity spectra (fit 2). All parameters, except T and V_{CN}, are given in eV.

Parameter	This Work	DFT Calculation (Ref. 41)
γ_0	3.16 ± 0.03	2.598 ± 0.015
γ_1	0.381 ± 0.003	0.34 ± 0.02
γ_3	0.38 ± 0.06	0.32 ± 0.02
γ_4	0.14 ± 0.03	0.177 ± 0.025
Δ	0.022 ± 0.003	0.024 ± 0.01
Γ	0.018 ± 0.003	
T	120 ± 15 K	
V_{CN}	-22 ± 1 V	

view is given, for example in Ref. 18). The agreement is good, except for γ_0, for which the DFT values are somewhat lower. Nevertheless, γ_0 deduced from various experiments on graphite[25] is in an excellent agreement with our result. Based on the obtained value of γ_0, we find the Fermi velocity $v_F=(3/2)a\gamma_0/\hbar$ to be $1.02 \pm 0.01 \times 10^6$ m/s ($a=1.42$ Å is the nearest-neighbor interatomic distance).

The gate voltage corresponding to zero doping, V_{CN}, can be determined with a very good accuracy. As it was mentioned in Sec. II A, this value is slightly different from the one extracted from the simultaneous transport measurement. It is possible that in the case of large flakes and a nonoptimal geometry of electrical contacts, it gives a more accurate value than the one given by the maximum of the dc resistivity as it is not affected by the distribution of the measurement currents in the flake. Infrared spectroscopy can be used, therefore, as an independent indicator of the doping level.

We find the broadening Γ to be about 15–20 meV. This value is larger than the one reported in Ref. 18 ($\approx 0.02\gamma_1 = 8$ meV), which is perhaps due to a higher concentration of charging impurities (the ones that shift the charge-neutral point from the zero bias). At the same time the value is considerably smaller than the broadening of about 60 meV found in Ref. 22 on double-gated graphene, which is probably related to extra scattering and/or inhomogeneity introduced by the top gate.

At first, surprisingly, the deduced temperature of graphene T is on the order of 100 K, even though the substrate was kept at 10 K. Although the true graphene temperature may indeed be somewhat higher due to a weak thermal contact between the warped flake and the substrate, another plausible explanation is that this is an indication of the spatial inhomogeneity of the chemical potential. It is easy to see that if we neglect the change in the bands as a function of μ then a smearing of the chemical potential $\mu \to \mu \pm \delta\mu$ has almost the same effect in the Kubo formula as increasing the temperature ($k_B T_{eff} \sim \delta\mu$). Thus we get an upper limit of about 10 meV to the inhomogeneity of the chemical potential. It is worth emphasizing that the thermal and the scattering-induced broadening given by T and Γ, respectively, are clearly distinguishable by the fitting routine.

Figure 4(a) shows the extracted bandgap as a function of the gate voltage and doping. Here we take $|U|$ as a measure

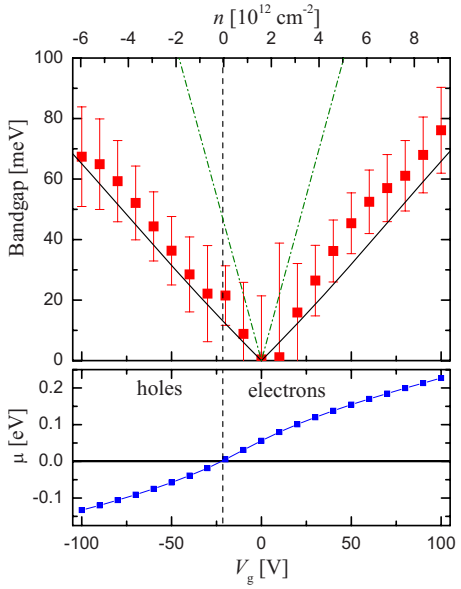

FIG. 4. (Color online) The extracted values of $|U|$ (top panel) and the chemical potential (bottom panel) as functions of the gate voltage and doping. Dash-dotted line—the calculated "unscreened" value of $|U|$, solid line—an *ab initio* DFT calculation from Ref. 42, which takes screening effects into account.

of the bandgap, since it practically coincides with Δ_g in the considered doping range. One can see that at small gate voltages the bandgap goes to zero within error bars and it grows almost linearly for both electron and hole doping, reaching 70–80 meV at the maximum applied gate voltages. Interestingly, the minimum is closer to zero-gate voltage (where $n \approx 2 \times 10^{12}$ cm^{-2}) than to $V_g=V_{CN}(n=0)$. As discussed by Castro *et al.*,[7] such a shift can be understood by considering the dopant molecules adsorbed by the surface acting as an effective top-gate electrode. However, in this case, the zero-gap point is expected to be at $V_g=-V_{CN}$. Seeing zero gap at zero-gate voltage would be expected if the dopants are intercalated between the carbon layers, so that they do not introduce an interlayer electrostatic asymmetry, however, we do not have any independent experimental verification of this happening. If the dopants were below the flake, in this picture one expects the gap to vanish at the charge-neutral point.

From Fig. 4(b) one can see that the chemical potential shows a monotonic, slightly sublinear increase with doping. In Fig. 5 the calculated band structures corresponding to the gate voltages −100, −20, 0, and +100 V are presented together with the position of the chemical potential.

B. Optical conductance

Figure 3(c) shows the real part of the optical conductance $G(\omega)$ calculated using the obtained tight-binding parameters as described above. As in Fig. 3(a), green solid and red dashed lines correspond to the fits 1 and 2, respectively. The conductance is normalized by $2G_0$, which is the theoretical asymptotic value for bilayer graphene at high frequencies.[27,28] One can see that the model curve corresponding to fit 1 shows a very broad γ_1 at positive gate

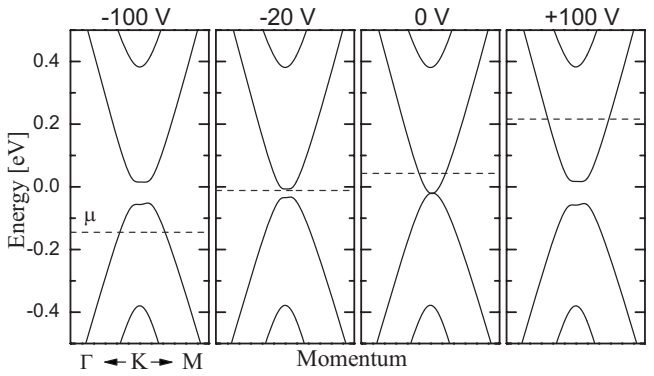

FIG. 5. Electronic bands (calculated using parameters extracted from optical spectra) and chemical potential at selected gate voltages.

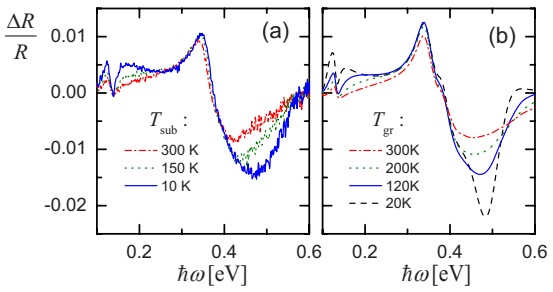

FIG. 6. (Color online) (a) The difference reflectivity at $V_g = -45$ V at three temperatures of the substrate: 300, 150, and 10 K. (b) Model curves of the same quantity calculated by varying the effective temperature of graphene and keeping other parameters unchanged (shown in Table I).

voltages because the parameter γ_3 in this fit was unrealistically large, as discussed above.

Since some deviations between the model fits and the experiment are present, we refined optical conductance using the Kramers-Kronig constrained variational method.[43] Within this approach, we represented the conductance as a sum of the two terms: $G(\omega)=G_{mod}(\omega)+G_{var}(\omega)$. The model term is calculated using Eqs. (2)–(4). $G_{var}(\omega)$ is a variational Kramers-Kronig constrained correction needed to reproduce all remaining fine detail of the experimental reflectivity spectra.[43] At the refinement stage, $G_{mod}(\omega)$ was fixed and $G_{var}(\omega)$ was adjusted in order to get the perfect match to the reflectivity spectra. The refined conductivity is shown in Fig. 3(c) with symbols. Since we based our analysis on the relative reflectivity spectra, this procedure gives most accurately the *relative* changes in $G(\omega)$ as a function of V_g and ω (the accuracy is better than $0.1G_0$), while the error bars for the absolute level of $G(\omega)$ can be somewhat larger. This explains slightly negative values of Re $G(\omega)$ at low frequencies at high-gate voltages. Weak structures below 0.15 eV are artifacts coming from the optical phonons in SiO_2, which are not fully cancelled in the fitting procedure, probably due to a weak dependence of these phonons on the electric field, which is not included in our model.

C. Temperature dependence

In addition to tuning the spectra by the gate voltage, varying the temperature provides another important piece of information. As an example, Fig. 6(a) shows $\Delta R(\omega, -45\ \text{V})/R$ taken at the *substrate* temperature T_{sub} of 10, 150, and 300 K. The spectra clearly change with cooling down. In general, the structures are getting sharper at low temperatures. However, the sharpening is far from being simply a uniform broadening such as due the electronic scattering (parameter Γ). In particular, the peak at 0.35 eV does not change, while both the dip at 0.45 eV and a structure at 0.2 show a pronounced temperature variation.

Panel (b) shows calculations of the same quantity at the following set of *graphene* temperatures: 20, 120, 200, and 300 K. In all cases, the same parameters, except T, were used (Table I). The calculated temperature dependence reproduces very well the experimental one if one assumes that the effective temperature of graphene is higher than T_{sub}. As we discussed above, this temperature mismatch may be in part due to the spatial broadening of the chemical potential. One can see that at $T=20$ K (dashed line), the spectral structures are expected to be much sharper than at 120 K. Similar spectra comparisons at other gate voltages (not shown) provide the same results.

The observation that the effect of temperature on the spectra is highly frequency selective is explained by the fact that only electronic transitions, for which either initial or the final state are close to the Fermi level, are affected by the temperature. As one can anticipate from the good match between spectra in panels (a) and (b) of Fig. 6, the application of the same least-square fitting procedure at higher temperatures provides model parameters, which are essentially the same as the ones presented. Therefore, we focus largely on the low-temperature results. Nevertheless, the ability to quantitatively predict spectra at high temperatures based on the results obtained at low temperature corroborates the consistency of the used model approach.

IV. DISCUSSION

A. Seeing bandgap optically: Zero versus finite doping

Optical spectroscopy is routinely used for the bandgap measurements in usual semiconductors due to the fact that only the photons, which energy exceeds the bandgap, are absorbed by electron-hole excitations. However, bilayer graphene is special in a sense that the bandgap is not intrinsic but is induced by the gate voltage. Therefore, if only one gate is attached to the flake, as in the present case, then the gap opening is inevitably accompanied by doping. Making two gate electrodes (on top and on bottom) would induce the bandgap without doping.[8] Figure 7 demonstrates, using a simplified set of SWMcC parameters, the effect of the bandgap in both cases. The bottom panel corresponds to the undoped case ($\mu=0$). One can see that an infrared-absorption threshold appears at $\hbar\omega \approx \Delta_g$, due to the transitions between the bands 2 and 3 across the bandgap (the bands are numbered in the inset). Such a structure was observed indeed in a recent paper by Zhang *et al.*,[22] who used a double-gate bilayer graphene device. The second notable effect is a shift by

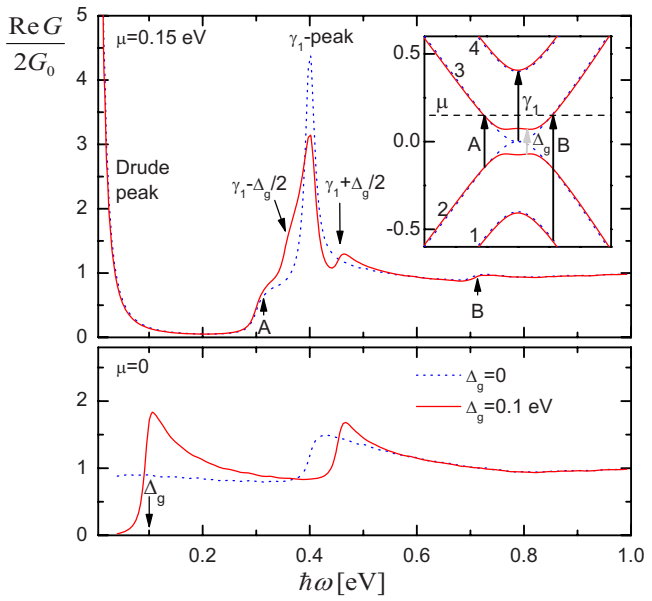

FIG. 7. (Color online) Model demonstration of the effect of the bandgap on optical spectra in the case of finite doping and the case of zero doping. Top panel: the chemical potential is larger than the bandgap; bottom panel: μ is zero. The inset shows the corresponding bands (energy, in eV, vs momentum near the K point). A simplified set of SWMcC parameters is used: $\gamma_0=3$ eV, $\gamma_1=0.4$ eV, and $\gamma_3=\gamma_4=\Delta=0$. The broadening Γ is 0.01 eV.

$\Delta_g/2$ of the second threshold at γ_1 corresponding to the transitions between bands 1 and 3 and also to ones between bands 2 and 4.

The top panel describes the case of a finite chemical potential (electron doping). There is a striking difference between the two cases. Now the opening of the gap does not produce an absorption threshold, since the transitions across the gap are blocked by the Pauli principle. However, the gap affects the line shape of the γ_1 peak that originates from a combination of interband transitions $3\rightarrow4$ and $2\rightarrow4$. Most notably, a satellite peak at about $\gamma_1+\Delta_g/2$ shows up. In addition, a shoulder at about $\gamma_1-\Delta_g/2$ appears. The satellite and the shoulder stem from the transitions $2\rightarrow4$ and $3\rightarrow4$, respectively, close to the K point, where they are separated by the bandgap energy. Thus, in the doped case the only way to measure the bandgap is to analyze the shape of the γ_1 peak.

In reality, the position and the shape of the peak are also affected by the parameters γ_3, γ_4, and Δ, not included in the above demonstration, and further broadened by electronic scattering. Therefore, when the gap is small, its extraction from the optical spectra requires direct fitting of the data using a complete set of SWMcC parameters. When the gap is large, the identification of the gap becomes easier as the satellite to the main peak is more pronounced. We note that in actual data one can clearly recognize a satellite to the γ_1 peak for $V_g \geq 80$ V [shown by arrows in Fig. 3(c)].

Although the fit reveals the presence of the bandgap also at negative gate voltages [Fig. 4(a)], the conductance spectra do not show a clear satellite at this doping side. Such a difference is in part due to the electron-hole asymmetry, which results in a stronger broadening of the γ_1 peak at the hole doping, and in part due to the shift in the charge neutrality point. However, in Sec. IV C we shall demonstrate direct signatures of the bandgap for both polarities of the gate voltage.

B. Bandgap: The role of self-screening

As discussed in Sec. II C, the bandgap is determined by the parameter U, which is defined as the difference in the electrostatic potential on the two layers. As it was extensively discussed in the literature,[6,7,18,44–46] the self-screening of the external field plays a crucial role in the determination of U. Our data fully agree with this. One can see (Fig. 4) that the experimental value of the bandgap is more than two times smaller than the "unscreened value" (dashed-dotted line), given by the external field multiplied by the interlayer distance (3.35 Å) (Ref. 42) (we assumed that the bandgap vanishes at $V_g=0$, based on the experimental results, which means that charging impurities do not introduce any imbalance of the interlayer potential). The same observation was made in Ref. 22

A proper microscopic calculation of the bandgap must be done self-consistently, since the screening depends on the bandgap and vice versa. Such a complicated problem was treated on the Hartree level based on the tight-binding model[6,7,18,46] as well as using *ab initio* methods.[42,44,45] These calculations provide the doping-dependent bandgap, which is much closer[47] to the present experiment than the "unscreened" model. As an example, we present in Fig. 4 the *ab initio* DFT calculation of Gava *et al.*[42] (solid line), which shows a good agreement with the experimental data.

C. "Photon energy—gate voltage" mapping of the interband transitions

We saw that the extraction of the optical conductance from the measured spectra is rather involved in the present case, where the measured spectra depend on both real and imaginary parts of $G(\omega)$ (as detailed in the Appendix). Now we propose a simple way to visualize electronic transitions based on the *raw* reflectivity data, which most clearly demonstrates the electron-hole asymmetry, the opening of the bandgap, and other features of the band structure.

In Fig. 8(a), the whole set of experimental spectra $\Delta R/R$ is represented as a color map in the coordinates $(\hbar\omega; V_g)$. One can see a set of lines that resemble somewhat band dispersions seen in ARPES. First we note the two "<"-like structures, shifted with respect to each other along the photon energy axis. They correspond to the onsetlike features in the optical conductance, marked in Fig. 7 as A and B and related to the interband transitions $2\rightarrow3$ and $1\rightarrow3$, respectively ($2\rightarrow3$ and $2\rightarrow4$ in the case of hole doping). Indeed, one can see that they match closely the expected threshold energies $\omega_A(V_g)=2|\mu(V_g)|$ (dashed line) and $\omega_B(V_g)=\gamma_1+2|\mu(V_g)|$ (dotted line). Although several experimental papers presented infrared spectra of gated bilayer graphene,[16,17,19–22] the second threshold was reported only in Ref. 20. Here we reaffirm, based on a new set of data, the existence of the second threshold, which is essential for the overall consistency of the tight-binding approach.

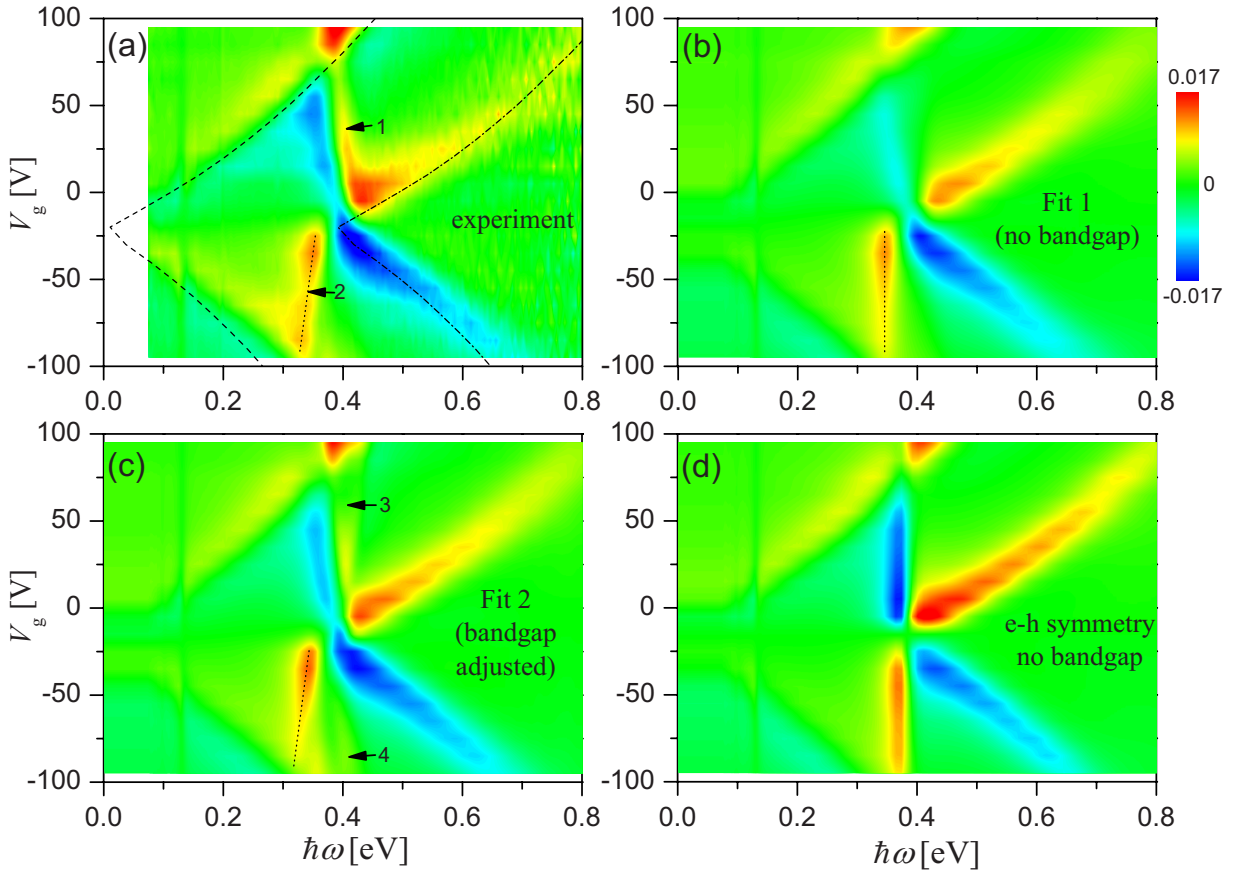

FIG. 8. (Color online) Color maps of $(\Delta R/R)(\omega, V_g)$. (a)—experiment, (b)—model curves corresponding to Fit 1 (zero bandgap), (c)—model curves corresponding to Fit 2 (including bandgap), and (d)—model curves in the absence of the bandgap and electron-hole asymmetry. The color scheme is the same in all graphs. The dashed and dash-dotted lines in panel (a) are the dependencies of $\omega_A = 2|\mu|$ and $\omega_B = \gamma_1 + 2|\mu|$, respectively.

In Fig. 8(a) the presence of electron-hole asymmetry is quite obvious, since in the case of perfectly symmetric bands with respect to the Dirac point the $\Delta R/R$ spectra should be precisely *antisymmetric* with respect to $V_g = V_{CN}$, as exemplified in the hypothetical graph of Fig. 8(d). Within the SWMcC model, the asymmetry between electron and holes bands is due to the hopping term γ_4 and the on-site energy difference Δ. In Refs. 18 and 19 they were deduced from the doping dependence of the position of the maximum of the γ_1 peak. Since the maximum location is affected not only by γ_1, γ_4, and Δ but also by γ_3, Γ, and, most importantly, by U, we choose to determine all parameters, including γ_4 and Δ, by fitting of the whole set of spectra.

This way of presenting spectra also allows us to see the distinct features related to the opening of the bandgap. These features appear to be quite different on the two doping sides due to the electron-hole asymmetry. In panels (b) and (c) of the same figure, we show the fits of $\Delta R/R$ without and with the bandgap, respectively (namely, fits 1 and 2 described in Sec. III A). On the electron side ($V_g > V_{CN}$) the "ridge" indicated as "1" finds absolutely no counterpart in fit 1, but is mimicked by in fit 2. On the hole side, the ridge marked as "2" clearly disperses toward low frequencies as the absolute value of V_g is increasing. This trend is well captured by fit 2, while in fit 1 this ridge is precisely vertical.

D. Deficiencies of the tight-binding description with constant scattering

Although the overall agreement between the panels (a) and (c) of Fig. 8 is very good, a closer inspection reveals some deficiencies in fit 2. For the electron doping, at gate voltages between 50 and 80 V, the ridge indicated by 1 is quite narrow in the experiment but is broad and barely recognizable in fit 2 (as indicated by 3 in panel (c). For the hole doping, fit 2 contains a weak extra ridge (marked as "4") which is not clearly present in the experiment. In Fig. 9 we concentrate on these doping levels, taking the gate voltages $V_g = -95$ V and +65 V as examples. Here we improved the

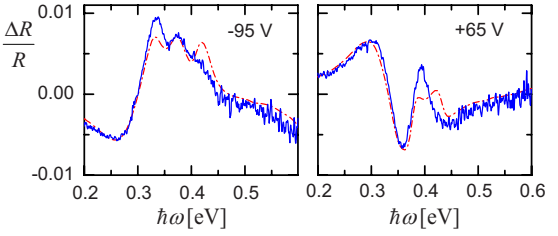

FIG. 9. (Color online) The experimental curves $(\Delta R/R)(\omega)$ (solid lines) at $V_g = -95$ V (left panel) and +65 V (right panel), together with the best fitting curves (dash-dotted lines).

match even further as compared to Fig. 3(b) by slightly compromising the fit quality at other gate voltages (although all the bandgaps were kept the same).

The model curve at −95 V is featured by three distinct peaks between 0.3 and 0.45 eV. Crudely speaking, they are related, respectively, to the shoulder, the main maximum and the satellite to the γ_1 peak depicted in Fig. 7. The value of U is related to but somewhat smaller than the distance between the leftmost and the rightmost peaks. We can see that the data also show three peaks at same photon energies, but the first peak is stronger and the third one is much weaker than the counterpart on the theoretical curve [the latter one gives rise to the feature "4" in Fig. 9(c)].

At V_g=+65 V the peak at 0.4 eV is rather sharp in the experiment but has a pronounced double structure in the model. Although this does not question the existence of the bandgap as such (recall that the best fit without the bandgap does not show this peak at all), such a discrepancy is too significant to be ignored.

Presently, the origin of the shown mismatches is not clear. This may be an indication that more hopping terms need to be taken into account. In this respect, it would be instructive to compare optical spectra directly to the results of *ab initio* band-structure calculations. Another possibility is that the discrepancies are caused by our assumption that the scattering Γ is the same for all electronic states, which can fail due to the electron-phonon and electron-electron interactions. Last but not least we have assumed in our analysis a rigid-band model, i.e., the tight-binding band parameters (apart from the bandgap) are assumed to be independent of doping and gate voltages. That this may not be strictly the case was experimentally shown in an ARPES study on epitaxial graphene,[9] where an increase in γ_1 by about 3% was observed when U changed from 0 to 100 meV. Electron-correlation effects introduce a doping and energy-dependent renormalization of the bare dispersion. Also the gate voltages influence the interatomic tunneling matrix elements, which in turn affect the tight-binding parameters. Studying the manifestation of these interactions in optical spectra will undoubtedly be one of the most intriguing directions in the further research of graphene.

V. SUMMARY

We presented a detailed analysis of infrared reflectivity spectra of bottom-gated bilayer graphene that allowed us to determine the tight-binding Slonczewski-Weiss-McClure parameters and the doping dependence of the bandgap induced by the electric field generated by the gate. The direct least-square fitting of the whole set of infrared spectra using the SWMcC Hamiltonian and the Kubo formula turns out to be a very efficient technique to disentangle the complicated interplay of various band-structure parameters in the optical spectra. It also provides independent information about the extrinsic doping level.

Our analysis clearly shows the presence of the bandgap, which depends almost linearly on the gate voltage. This dependence agrees with the tight-binding and *ab initio* calculations that take the screening of the external field by the π bands into account. At the maximum applied gate voltage of 100 V the bandgap reaches about 80 meV, which is three times larger than k_BT at room temperature. Even higher values of the bandgap (up to 250 meV) could be obtained on double-gated bilayer graphene,[22] making this material very promising for applications.

The very fact of achieving quantitatively good fits is a strong indication that the tight-binding model is quite accurate for the actual band structure of bilayer graphene. Nevertheless, some discrepancies remain, and further investigations will be needed to explore their origin in the context of electron-phonon and electron-electron interactions.

ACKNOWLEDGMENTS

We are grateful to A. K. Geim, A. H. MacDonald, F. Mauri, E. McCann, L.A. Falkovsky, and D.N. Basov for illuminating discussions. This work was supported by the Swiss National Science Foundation (SNSF) under the Grant No. 200021-120347, through the National Center of Competence in Research "Materials with Novel Electronic Properties-MaNEP."

APPENDIX: RELATION BETWEEN THE REFLECTIVITY AND THE OPTICAL CONDUCTANCE OF GRAPHENE

The reflectivity of bare substrate, and graphene on top of the substrate [Fig. 1(a)] can be calculated based on the optical conductance of graphene $G(\omega)$ and the known dielectric functions $\epsilon(\omega)$ of SiO_2 and Si.[30,31] We can treat the silicon layer as semi-infinite, since in our case it is thicker than the penetration depth. The Fresnel equations for the reflectivities can be written as follows:

$$R_{sub} = \left| r_{01} + \frac{t_{01}t_{10}\phi^2}{1 - r_{10}r_{12}\phi^2} \right|^2, \tag{A1}$$

$$R_{gr} = \left| \tilde{r}_{01} + \frac{\tilde{t}_{01}\tilde{t}_{10}\phi^2}{1 - \tilde{r}_{10}r_{12}\phi^2} \right|^2, \tag{A2}$$

where indices 0,1, and 2 refer to vacuum (ϵ=1), SiO_2, and Si layers, respectively, and

$$\phi = \exp\left(i\frac{\omega}{c}\sqrt{\epsilon_1}d_1 \right). \tag{A3}$$

We used the complex reflection and transmission coefficients at the interface between media i and j

$$r_{ij} = \frac{\sqrt{\epsilon_i} - \sqrt{\epsilon_j}}{\sqrt{\epsilon_i} + \sqrt{\epsilon_j}}, \tag{A4}$$

$$t_{ij} = \frac{2\sqrt{\epsilon_i}}{\sqrt{\epsilon_i} + \sqrt{\epsilon_j}}. \tag{A5}$$

The presence of graphene between layers (in our case it is between vacuum and SiO_2) modifies the interface coefficients in the following way:

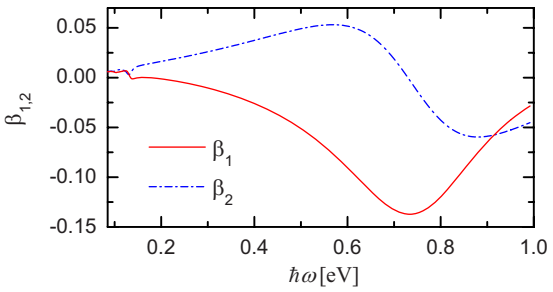

FIG. 10. (Color online) The functions $\beta_1(\omega)$ and $\beta_2(\omega)$, describing the sensitivity of $(\Delta R/R)(\omega)$ to $\Delta G_1(\omega)$ and $\Delta G_2(\omega)$, respectively (obtained at 10 K).

$$\tilde{r}_{ij} = \frac{\sqrt{\epsilon_i} - \sqrt{\epsilon_j} - \pi\alpha\frac{G}{G_0}}{\sqrt{\epsilon_i} + \sqrt{\epsilon_j} + \pi\alpha\frac{G}{G_0}}, \tag{A6}$$

$$\tilde{t}_{ij} = \frac{2\sqrt{\epsilon_i}}{\sqrt{\epsilon_i} + \sqrt{\epsilon_j} + \pi\alpha\frac{G}{G_0}}, \tag{A7}$$

where $\alpha = e^2/\hbar c$ is the fine-structure constant. The latter formulas are valid in the thin-film limit (the thickness is much smaller than the wavelength), which is perfectly applicable to graphene.

Since the typical values $\Delta R/R$ [Fig. 3(b)] are rather small ($\sim 10^{-2}$), it is useful to introduce the so-called "sensitivity" functions that we previously used in similar analyses[48,49] and employ an approximate linear relation

$$\frac{\Delta R(\omega)}{R} \approx \beta_1(\omega)\frac{\mathrm{Re}\,\Delta G(\omega)}{G_0} + \beta_2(\omega)\frac{\mathrm{Im}\,\Delta G(\omega)}{G_0}. \tag{A8}$$

Here we obtained the sensitivity functions $\beta_1(\omega)$ and $\beta_2(\omega)$ numerically, using a linear regression of the exact formulas for the values of $G/G_0 \sim 1$. These functions, which are specific to the substrate used are shown in Fig. 10. One can see that the reflectivity depends on both the real and the imaginary parts of $G(\omega)$ in a nontrivial way. At high energies, the dependence is stronger than at low energies. Optical phonons in SiO_2 give rise to structures at ~ 0.15 eV, which affect $\Delta R/R$.

[1] K. S. Novoselov, A. K. Geim, S. V. Morozov, D. Jiang, M. I. Katsnelson, I. V. Grigorieva, S. V. Dubonos, and A. A. Firsov, Nature (London) **438**, 197 (2005).
[2] Y. Zhang, Y. W. Tan, H. L. Stormer, and P. Kim, Nature (London) **438**, 201 (2005).
[3] K. S. Novoselov, E. McCann, S. V. Morozov, V. I. Fal'ko, M. I. Katsnelson, A. K. Geim, F. Schedin, and D. Jiang, Nat. Phys. **2**, 177 (2006).
[4] E. McCann and V. I. Fal'ko, Phys. Rev. Lett. **96**, 086805 (2006).
[5] J. Nilsson, A. H. Castro Neto, F. Guinea, and N. M. R. Peres, Phys. Rev. B **76**, 165416 (2007).
[6] E. McCann, Phys. Rev. B **74**, 161403(R) (2006).
[7] E. V. Castro, K. S. Novoselov, S. V. Morozov, N. M. R. Peres, J. M. B. Lopes dos Santos, J. Nilsson, F. Guinea, A. K. Geim, and A. H. Castro Neto, Phys. Rev. Lett. **99**, 216802 (2007).
[8] J. B. Oostinga, H. B. Heersche, X. Liu, A. F. Morpurgo, and L. M. K. Vandersypen, Nature Mater. **7**, 151 (2008).
[9] T. Ohta, A. Bostwick, T. Seyller, K. Horn, and E. Rotenberg, Science **313**, 951 (2006).
[10] V. Ryzhii, M. Ryzhii, Y. Hu, I. Hagiwara, and M. S. Shur, Appl. Phys. Lett. **90**, 203503 (2007).
[11] Y. M. Lin, K. A. Jenkins, A. Valdes-Garcia, J. P. Small, D. B. Farmer, and P. Avouris, Nano Lett. **9**, 422 (2009).
[12] G. Fiori and G. Iannaccone, IEEE Electron Device Lett. **30**, 261 (2009).
[13] K. Novoselov, A. Geim, S. Morozov, D. Jiang, Y. Zhang, S. Dubonos, I. Grigorieva, and A. Firsov, Science **306**, 666 (2004).
[14] Z. Q. Li, E. A. Henriksen, Z. Jiang, Z. Hao, M. C. Martin, P. Kim, H. L. Stormer, and D. N. Basov, Nat. Phys. **4**, 532 (2008).
[15] Z. Jiang, E. A. Henriksen, L. C. Tung, Y. J. Wang, M. E. Schwartz, M. Y. Han, P. Kim, and H. L. Stormer, Phys. Rev. Lett. **98**, 197403 (2007).
[16] E. A. Henriksen, Z. Jiang, L. C. Tung, M. E. Schwartz, M. Takita, Y. J. Wang, P. Kim, and H. L. Stormer, Phys. Rev. Lett. **100**, 087403 (2008).
[17] F. Wang, Y. Zhang, C. Tian, C. Girit, A. Zettl, M. Crommie, and Y. R. Shen, Science **320**, 206 (2008).
[18] L. M. Zhang, Z. Q. Li, D. N. Basov, M. M. Fogler, Z. Hao, and M. C. Martin, Phys. Rev. B **78**, 235408 (2008).
[19] Z. Q. Li, E. A. Henriksen, Z. Jiang, Z. Hao, M. C. Martin, P. Kim, H. L. Stormer, and D. N. Basov, Phys. Rev. Lett. **102**, 037403 (2009).
[20] A. B. Kuzmenko, E. van Heumen, D. van der Marel, P. Lerch, P. Blake, K. S. Novoselov, and A. K. Geim, Phys. Rev. B **79**, 115441 (2009).
[21] K. F. Mak, C. H. Lui, J. Shan, and T. F. Heinz, Phys. Rev. Lett. **102**, 256405 (2009).
[22] Y. Zhang, T.-T. Tang, C. Girit, Z. Hao, M. C. Martin, A. Zettl, M. F. Crommie, Y. R. Shen, and F. Wang, Nature (London) **459**, 820 (2009).
[23] J. W. McClure, Phys. Rev. **108**, 612 (1957).
[24] J. C. Slonczewski and P. R. Weiss, Phys. Rev. **109**, 272 (1958).
[25] M. S. Dresselhaus and G. Dresselhaus, Adv. Phys. **30**, 139 (1981).
[26] J. Nilsson, A. H. Castro Neto, F. Guinea, and N. M. R. Peres, Phys. Rev. Lett. **97**, 266801 (2006).
[27] D. S. L. Abergel and V. I. Fal'ko, Phys. Rev. B **75**, 155430 (2007).
[28] E. J. Nicol and J. P. Carbotte, Phys. Rev. B **77**, 155409 (2008).
[29] F. Schedin, A. K. Geim, S. V. Morozov, E. W. Hill, P. Blake, M. I. Katsnelson, and K. S. Novoselov, Nature Mater. **6**, 652 (2007).
[30] P. Blake, K. S. Novoselov, A. H. C. Neto, D. Jiang, R. Yang, T. J. Booth, A. K. Geim, and E. W. Hill, Appl. Phys. Lett. **91**,

063124 (2007).
[31] D. S. L. Abergel, A. Russell, and V. I. Fal'ko, Appl. Phys. Lett. **91**, 063125 (2007).
[32] A. B. Kuzmenko, L. Benfatto, E. Cappelluti, I. Crassee, D. van der Marel, P. Blake, K. S. Novoselov, and A. K. Geim, Phys. Rev. Lett. **103**, 116804 (2009).
[33] A. H. CastroNeto, F. Guinea, N. M. R. Peres, K. S. Novoselov, and A. K. Geim, Rev. Mod. Phys. **81**, 109 (2009).
[34] C. L. Lu, C. P. Chang, Y. C. Huang, R. B. Chen, and M. L. Lin, Phys. Rev. B **73**, 144427 (2006).
[35] T. Ando, Y. Zheng, and H. Suzuura, J. Phys. Soc. Jpn. **71**, 1318 (2002).
[36] V. P. Gusynin, S. G. Sharapov, and J. P. Carbotte, Phys. Rev. Lett. **96**, 256802 (2006).
[37] L. A. Falkovsky and A. Varlamov, Eur. Phys. J. B **56**, 281 (2007).
[38] R. R. Nair, P. Blake, A. N. Grigorenko, K. S. Novoselov, T. J. Booth, T. Stauber, N. M. R. Peres, and A. K. Geim, Science **320**, 1308 (2008).
[39] A. B. Kuzmenko, E. van Heumen, F. Carbone, and D. van der Marel, Phys. Rev. Lett. **100**, 117401 (2008).
[40] W. H. Press, B. P. Flannery, S. A. Teukolsky, and W. T. Vetterling, *Numerical Recipes: The Art of Scientific Computing*, 3rd ed. (Cambridge University Press, Cambridge, 2007).
[41] J. C. Charlier, X. Gonze, and J. P. Michenaud, Phys. Rev. B **43**, 4579 (1991).
[42] P. Gava, M. Lazzeri, A. M. Saitta, and F. Mauri, Phys. Rev. B **79**, 165431 (2009).
[43] A. B. Kuzmenko, Rev. Sci. Instrum. **76**, 083108 (2005).
[44] M. Aoki and H. Amawashi, Solid State Commun. **142**, 123 (2007).
[45] H. Min, B. Sahu, S. K. Banerjee, and A. H. MacDonald, Phys. Rev. B **75**, 155115 (2007).
[46] L. A. Falkovsky, arXiv:0905.1765 (unpublished).
[47] In Eq. (5) of Ref. 6, setting $v_F = 1.02 \times 10^6$ m/s, $\gamma_1 = 0.38$ eV (as in the present paper), $\epsilon_r = 2.2$, and $\Delta_0 = -22$ V provides a very good match to the present experimental data (E. McCann, private communication).
[48] A. B. Kuzmenko, N. Tombros, H. J. A. Molegraaf, M. Gruninger, D. van der Marel, and S. Uchida, Phys. Rev. Lett. **91**, 037004 (2003).
[49] A. B. Kuzmenko, H. J. A. Molegraaf, F. Carbone, and D. van der Marel, Phys. Rev. B **72**, 144503 (2005).